

## A Piezoelectrical Rain Gauge for Application on Buoys

JÖRG FÖRSTER

*Forschungsanstalt der Bundeswehr für Wasserschall und Geophysik (FWG), Kiel, Germany*

GISELHER GUST

*Technische Universität Hamburg-Harburg, Hamburg, Germany*

SIEGFRIED STOLTE

*Forschungsanstalt der Bundeswehr für Wasserschall und Geophysik (FWG), Kiel, Germany*

(Manuscript received 8 November 2000, in final form 16 June 2003)

### ABSTRACT

Rain gauge systems are required to measure rainfall data on buoys at oceanic sites that are not suited for conventional rain sensors. A piezoelectrical rain gauge has been developed for use on buoys, to provide rain measurements just above the sea surface. Based on the piezoelectric effect, each drop is measured separately with regard to its size, which is derived from the momentum transfer function of the sensor. Thus, the characteristics of rain—for example, the momentum flux, the drop intensity, and the drop size distribution—can be determined. In addition to laboratory investigations, showing the principal applicability of spherical piezoelectrical ceramics for rain detection, and the calibration, a field experiment had been conducted, comparing the new rain sensor results with those of other conventionally used rain gauges (Joss–Waldvogel disdrometer, FM–CW Doppler radar, and a ship rain gauge). The results are in good agreement. Such devices are needed to obtain a better understanding of rain-induced sea surface processes like the damping of sea waves, the short-scale sea surface roughness enhancement, and the generation of ambient noise, all of which affect radar and acoustic remote sensing.

Roughness variations of the sea surface due to rain have been measured by a drifting buoy system. Using the piezoelectrical rain gauge, simultaneous in situ measurements of rain and rain-related sea surface variations have been performed. Results show a strong increase in the energy density spectra in the frequency band from 3 to 30 Hz, representing wavelengths between 17 and 0.7 cm, respectively. Therefore, the backscatter of X-, C-, and L-band radar wavelengths, which correspond to this range, are strongly affected by rain-induced sea surface roughness variations, especially in low-wind situations.

### 1. Introduction

As part of the hydrological cycle, rain is also of importance to the thermal budget of the atmosphere. For land-based investigations, rain gauges based on a variety of principles have been developed in the past (Joss and Waldvogel 1967; PMS 1989; Winkler 1993; Wang and Crosby 1993; Nystuen et al. 1996). Yet, the greatest amounts of precipitation occur over oceans. In these areas, conventional rain sensors can only be used on-board ships (Skaar 1955; Hasse et al. 1994, 1998). Especially for measurements close to the sea surface no suitable instruments were available until now. On the other hand, such devices are required to increase the knowledge of rain-related interfacial processes such as

wave damping or sea surface roughening under natural environmental conditions (Förster 1998, 1999).

Sea surface variations due to rain are closely related to the momentum flux, which mainly depend on the rain drop size distribution and the wind velocity.

Drop impingement on the water surface leads to several processes such as cavity and crown development, generating of canopies, jet formation, secondary droplet impingement, turbulence enhancement, bubble production, and noise generation, most of which only last milliseconds (Le Méhauté et al. 1987; Le Méhauté 1988; Hsiao et al. 1988; Pumphrey and Crum 1990; Bliven et al. 1997; Förster 1998, 1999; Craeye 1998).

The kinetic energy of drops is channelled into three portions.

First, the drop impact generates short gravity capillary ring waves. The ensuing horizontal propagation of energy in a radial direction accounts for approximately 25% of the impact kinetic energy (Förster 1998).

---

*Corresponding author address:* Dr. J. Förster, Forschungsanstalt der Bundeswehr für Wasserschall und Geophysik, Klausdorfer Weg 2-24, D-24148 Kiel, Germany.  
E-mail: foerster@fwg-kiel.de

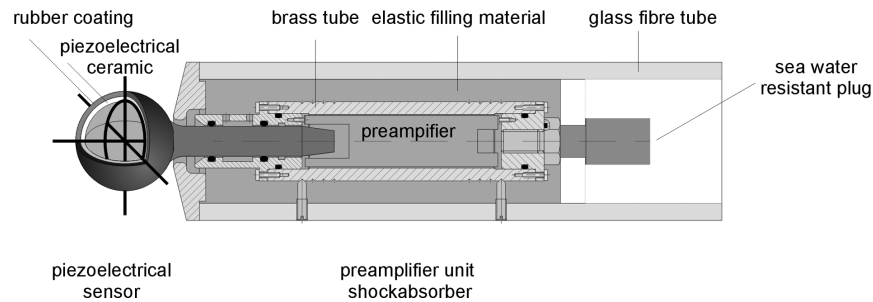


FIG. 1. Technical realization of the piezoelectrical rain gauge, optimized for applications on buoys. The physical principle of the rain sensor is based on the piezoelectrical effect, and ceramic material such as  $\text{Pb}(\text{Zr}, \text{Ti})\text{O}_3$  can be used for measuring external forces.

Second, impact-related turbulence leads to vertical energy propagation. This process dissipates about 75% of the energy entrained by drop impact (Förster 1998). Furthermore, it interacts with the ring waves and results in wave damping.

Third, a very small amount of the kinetic energy is converted into acoustical energy in the form of compressional waves. Although rain-generated noise is the dominant source of sound at the sea surface and exceeds the noise level of surface wave agitation up to 20 dB, the portion of the kinetic drop energy  $E_{\text{kin}}$  that is transferred to acoustical energy  $E_{\text{ac}}$  is less than 0.1‰ ( $E_{\text{ac}}/E_{\text{kin}} < 10^{-4}$ ) (Förster 1998).

In addition, rain intensifies the wind-induced shear stress acting on the sea surface. Especially in situations of low wind, high rain intensity has a significant effect on tangential stress enhancement (Caldwell and Elliott 1971; Förster 1998).

The objective of this paper is to present a novel rain gauge for applications on buoys, which responds to both horizontal and vertical rain impact. In addition to the physical principle of the method, which is based on the piezoelectrical effect, the calibration procedure of the

device is documented. Validation of the method had been performed during a field experiment in comparison with different conventional rain gauges. Based on the momentum transfer function of drops impinging on the piezoelectrical rain sensor, rain parameters such as drop number, rain rate, drop size distribution, and vertical and horizontal momentum fluxes can be estimated. For applications in rough oceanic conditions on a buoy system, the realization of the piezoelectrical rain gauge is presented. First results of in situ measurements, correlating rain rates with rain-induced sea surface roughness variations, prove the applicability of the new sensor. An appendix that provides the definitions of the notation used is provided.

## 2. Physical principle and design of the piezoelectrical rain sensor

### a. General

The physical principal of the spherical rain sensor shown in Fig. 1 is based on the piezoelectrical effect. A force  $F$  acting on the sensor surface generates a voltage output  $U$ , which is proportional to the acting force

$$U = \frac{d}{C_s} F, \quad (1)$$

where  $d$  is the piezoelectrical constant for normal acting forces and  $C_s$  the capacity of the sensor element. Typical values for the sensor ceramic material  $\text{Pb}(\text{Zr}, \text{Ti})\text{O}_3$  are  $d = 400 \text{ pC/N}$  and  $C_s = 30 \text{ nF}$  (Channel Industries, Inc. 1995).

Equation (1) has been verified by applying defined normal oriented forces to a spherically formed transducer. Based on the relation  $F_i = m_i g$ , defined forces  $F_i$  were generated by different weights (Förster 1998). As illustrated in Fig. 2, the outputs  $U_i$  are nearly proportional to the forces  $F_i$ . Linear regression yields a correlation coefficient  $r = 0.98$ . Based on this result, forces acting locally and normal to the sensor surface can be quantified. Additionally, the sensor outputs  $U_i$  have been measured for oblique acting forces. The result is in close agreement with a cosine approximation as

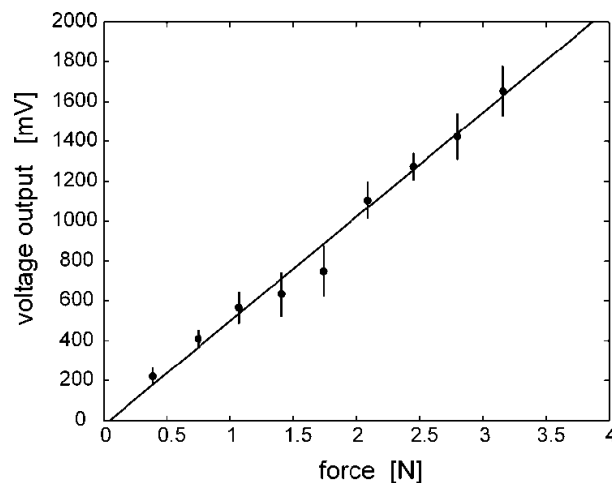


FIG. 2. Verification of the piezoelectrical effect by applying normal acting forces on a spherical ceramic sensor.

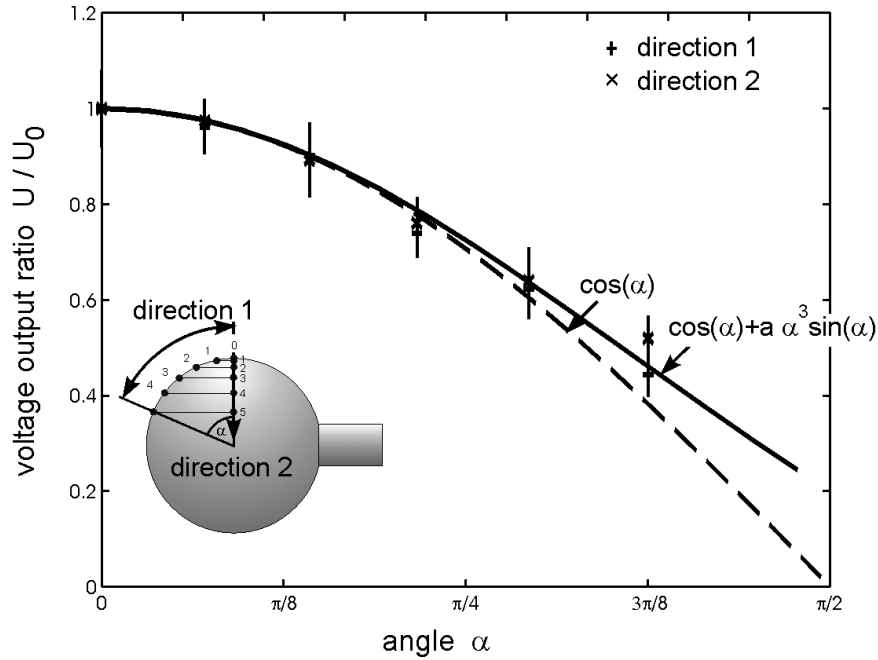


FIG. 3. Verification of the piezoelectrical effect by applying oblique and normal acting forces on a spherical ceramic sensor.

shown in Fig. 3. This sensor characteristic has to be taken into account when correlating sensor signals to drop-induced forces.

#### b. Calibration requirements

During drop impact the force  $F$  in Eq. (1) is a function of both drop size and impingement duration, that is, impact velocity. This time is nearly equivalent to the duration the drop needs to fall a distance equal to its diameter. Thus, in order to consider the total impact process, the integral value of Eq. (1) has to be taken into account. Time integration yields

$$\int U dt = \frac{d}{C_s} \int F dt = \frac{d}{C_s} \Delta p, \quad (2)$$

where  $\Delta p$  is the momentum due to the force  $F$  transferred by a drop. Since the drop momentum  $p$  is given by the velocity  $v$  and mass  $m$ , which are related to each other, the time integral of  $U$  is a measure of the drop diameter  $D$ . Based on the momentum transfer function  $f$ ,

$$f(D, v) = \int U(D, v) dt = \frac{d}{C} \int F dt \quad (3)$$

$$= \frac{d}{C} \text{ or } f(D, v)/\Delta p(D, v), \quad (4)$$

the drop size can be determined. To find the sensor-specific transfer function  $f(D, v)$  the sensor needs to be calibrated with drops of defined sizes and velocities, taking into account the statistical average over the impact angles (see section 4).

#### c. Rain and wind

Under natural conditions the drop impact velocity  $v_{\text{imp}}$  is given by the horizontal and vertical vector components  $v_{\text{hor}}$  and  $v_{\text{ver}}$ . While the horizontal component  $v_{\text{hor}}$  depends on the wind speed  $v_w$  (Caldwell and Elliott 1971), the vertical component  $v_{\text{ver}}$  is given by up- and downdrafts  $v_z$  and the terminal velocity  $v_{\text{term}}$ , which referring to Gunn and Kinzer (1949) and Atlas et al. (1973) increases with drop diameter  $D$

$$v_{\text{term}}(D) = 9.65 - 10.30e^{-0.6D}. \quad (5)$$

The momentum of a drop just before its impact is

$$p(D) = mv_{\text{imp}} = \frac{\pi}{6} \rho D^3 \sqrt{(v_{\text{term}} + v_z)^2 + v_{\text{hor}}^2}, \quad (6)$$

where  $\rho$  is the density of the fluid and  $v_{\text{hor}}$  the horizontal velocity, given by the wind speed  $v_w$ . For  $v_w = v_{\text{hor}} = v_z = 0$  the momentum increases nearly with  $D^{3.5}$  (Spilhaus 1948). For each wind velocity a defined relationship exists between drop momentum  $p$  and drop size  $D$ . Therefore, by measuring both wind velocities and drop-induced sensor signals, drop sizes can be deduced, when the spherical form of the rain sensor is considered.

### 3. Piezoelectrical rain gauge: Technical realization

The piezoelectrical rain gauge was developed for oceanic environments, especially for use on buoys to measure rain characteristics—for example, drop intensity (drops  $\text{s}^{-1} \text{m}^{-2}$ ), rain rate ( $\text{mm h}^{-1}$ ), drop size distribution, and momentum flux. The technical realization is sketched in Fig. 1.

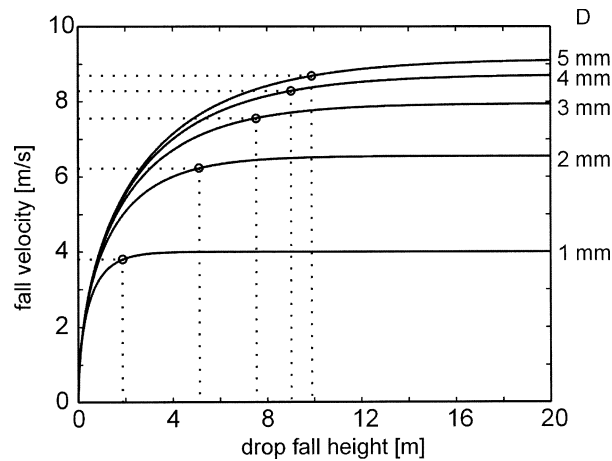


FIG. 4. Drop velocity increase with fall height for drop sizes between 1- and 5-mm diameter.

The sensor consists of a spherically formed piezoelectrical ceramic used in conventional hydrophones. It is based on a sensor type S-1012-1.5" (Ocean Research Technology 1990). Embedded in a rubber coating, it is seawater resistant and suited for applications on buoys. The head is attached to a brass tube containing a pre-amplifier. To avoid shock waves from frame vibrations, which would enhance the noise level of the sensor, the brass tube was integrated in a shock absorber housing,

which consists of a second tube and elastic filling material. The characteristics of the sensor are the following.

- A rubber coating that provides seawater resistance and negligible fouling. This is a basic requirement for long-time reliable operation, even after contact with seawater by submergence and spray.
- A principle requiring no moving components. This is ideal for long time exposure without maintenance.

#### 4. Piezoelectrical rain gauge: Calibration

The sensor calibration was performed using defined drop sizes at wind speed  $v_w = 0 \text{ m s}^{-1}$ . A maximum fall height of 14 m guaranteed terminal velocity within 95%, based on the dependence of drop velocity  $v$  on fall height  $h$  and drop size  $D$  (Förster 1998). Taking into account the acceleration by gravity  $g$  and the drag force in air  $F_d = -\gamma(v^2)$  the following equation was derived:

$$v(h, D) = v_{\text{term}}/(D) \sqrt{1 - \exp\left[-\frac{2g}{v_{\text{term}}^2(D)}h\right]}, \quad (7)$$

where  $v_{\text{term}}$  is the terminal velocity according to Gunn and Kinzer (1949).

For drop sizes between 1 and 5 mm and heights up to 20 m, the increase of drop velocities is shown in Fig. 4. Speeds at 95% of corresponding terminal velocities

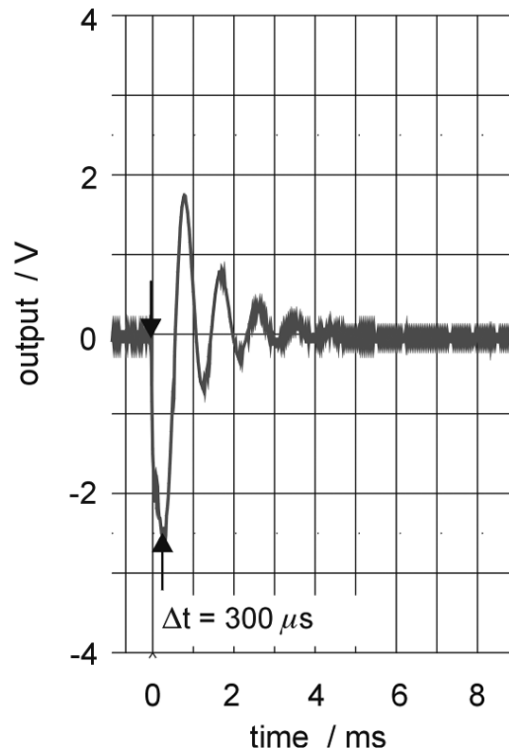
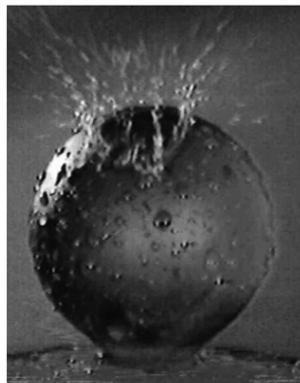


FIG. 5. (left) Impact of a 3.2-mm drop on the sensor surface with terminal velocity. (right) Time series of rectified sensor signal output. Here  $\Delta t = 300 \mu\text{s}$  relates to time increment from  $t = 0$  onward.

TABLE 1. Drop rate based on a MP drop size distribution.

Rain rate (mm h <sup>-1</sup> )	Normalized drop intensity (m <sup>-2</sup> s <sup>-1</sup> )	Drop intensity at the sensor area [(15.9 cm <sup>2</sup> ) <sup>-1</sup> s <sup>-1</sup> ]
100	11 632	18
12	4833	6
4.5	3133	3
0.75	1349	1

are marked on calculated curves. Thus, the fall height of 14 m was considered adequate to provide nearly natural drop impact conditions.

Drops of defined sizes were generated by a drop dispense unit. After release they were accelerated by gravity. To avoid drop displacement by air turbulence, the drops passed a tube of 13-m length before they hit the sensor element just beneath the lower end of the tube.

Drop impact processes last only milliseconds. To document details of impingement, a high-speed camera was operated at 500 frames per second. The filming of drop impacts on the sensor surface was synchronized with storage of digitized sensor signals (Förster 1998).

A typical drop impact is presented in Fig. 5. The photo shows the drop shortly after its impact at the sensor center, marked by the arrow in the signal time series at 300  $\mu$ s. Secondary droplets are pinched off from the rim of the wet area. The time series of the signal shows that the impacting process ended 300  $\mu$ s after the first contact. Afterward a sensor-specific damped oscillation persists up to 5 ms. This type of signal was reproduced for all drop impacts and represents the momentum transfer of the impinging drops. Thus a maximum number of about 200 drops per second is detectable by the sensor. But this saturation value will not be attained under normal environmental conditions, where a rain rate of 100 mm h<sup>-1</sup> corresponds to a drop intensity of about 11 632 drops s<sup>-1</sup> m<sup>-2</sup>, assuming a Marshall–Palmer exponential drop size distribution (Marshall and Palmer 1948, see Table 1). This drop intensity corresponds to 18 drops per second per sensor cross section of 15.9 cm<sup>2</sup>. Only for very extreme rain rates (>100 mm h<sup>-1</sup>) do statistical corrections to the drop size distribution need to be taken into account to consider the dead time of the instrument (5 ms per drop impact).

The calibration procedure of the piezoelectrical rain gauge was performed by generating five specific drop sizes with diameters of 2.3, 2.9, 3.2, 4.0, and 5.0 mm.

TABLE 2. Fall height–drop size combinations used for rain gauge calibration.

Height (m)	Drop diameter (mm)				
	2.3	2.9	3.2	4.0	5.0
3.65	+	+	+	+	+
8.23	–	+	+	+	+
14.70	–	–	+	+	+

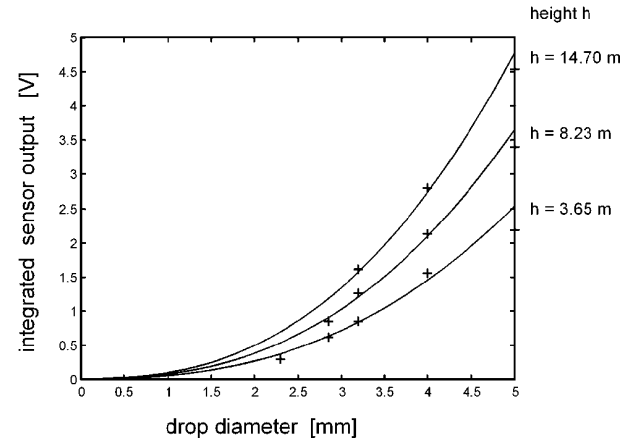


FIG. 6. Means of integrated sensor signals (+) caused by central drop impacts on a piezoelectrical rain gauge. Power approximations according to Eq. (8) are presented.

Combinations of fall heights and drop sizes that had been selected in the experiment are given in Table 2.

For each fall height and drop size about 400 impacts were recorded. Rectified sensor signals as shown in Fig. 5 were integrated and mean results of central drop impacts are shown in Fig. 6. They were approximated by a power function:

$$U_{\text{int}} = aD^{2.5}. \quad (8)$$

The coefficient ( $a$ ) increases with fall height (Table 3).

The upper line in Fig. 6 is the sensor calibration curve for stagnant air condition  $v_w = 0$  m s<sup>-1</sup> at terminal drop velocity. Although as stated above the momentum of a drop just before its impact should be proportional to  $D^{3.5}$ , this is not necessarily the amount of momentum being transferred to the sensor during the impacting process, as the impinging drop separates in several secondary droplets (Fig. 5), all of which remain some small part of the initial momentum. Due to this fact the empirically deduced signal proportionality of  $D^{2.5}$  in Eq. (8) deviates from the momentum proportionality of  $D^{3.5}$  for drops falling with terminal velocity.

To extrapolate sensor signals to windy conditions the increase of drop impact momentum with fall height was evaluated. Based on measurements at 8.23- and 14.70-m fall heights, the change of the integrated sensor signal  $\Delta U_{\text{int}}$  to that of the momentum  $\Delta p$  depends on drop size  $D$ :

$$\frac{\Delta U_{\text{int}}}{\Delta p}(D) = -0.0245D + 0.1415, \quad (9)$$

TABLE 3. Coefficient  $a$  in relation to fall height.

Height (m)	$a$
3.65	0.045
8.23	0.065
14.70	0.085

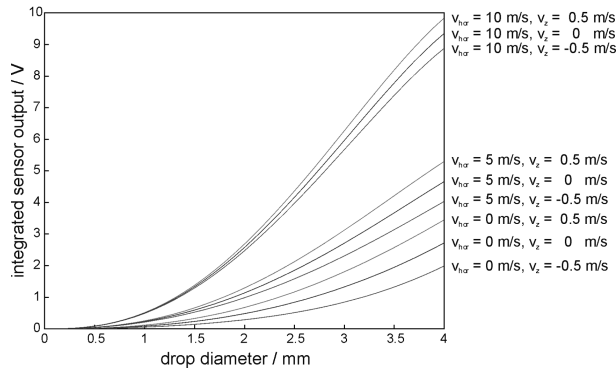


FIG. 7. Increase of integrated sensor signals caused by normal orientated drop impacts on a piezoelectrical rain gauge for wind speeds  $v_{\text{hor}} = 0, 5, \text{ and } 10 \text{ m s}^{-1}$  and up- and downdrafts  $v_z = -0.5, 0, \text{ and } +0.5 \text{ m s}^{-1}$ .

where  $\Delta p$  relates to the drop mass, the horizontal and vertical components of wind velocity  $v_{\text{hor}}, v_z$ :

$$\Delta p = m\Delta v = m(\sqrt{(v_{\text{term}} + v_z)^2 + v_{\text{hor}}^2} - v_{\text{term}}). \quad (10)$$

Utilizing Eqs. (9) and (10) the wind-induced effect on drop-generated sensor signals was estimated. For horizontal wind speeds  $v_{\text{hor}} = 0, 5, \text{ and } 10 \text{ m s}^{-1}$  and up-, downdrafts  $v_z = -0.5, 0, 0.5 \text{ m s}^{-1}$  the corresponding curves are given in Fig. 7.

Based on this momentum transfer function, mean rain

features can be deduced when taking into account the cosine sensitivity (Fig. 3) and a stationary uniform distribution of impacting drops over the sensor cross section during the basic recording time unit (1 min in our case).

In situ measurements of rain on our buoy system are therefore realized by simultaneous recordings of drop-induced sensor signals and wind velocity components using a sonic anemometer. The combination of Eqs. (8) and (9) only give the transfer function for perpendicular impacting drops influenced by wind. The spherical shape of the sensor is relevant for the fact that drop signals  $U$  are not only a function of size  $D$  and wind velocity  $v$ , but also of impact angle  $\beta$ :  $U = U(D, v, \beta)$ , as illustrated in Fig. 8. The amplitude of a drop signal increases from a minimum value  $U_{\text{min}} = U(D, v, \beta \approx 0^\circ)$  for tangential impact to a maximum in the case of normal incidence  $U_{\text{max}} = U(D, v, \beta = 90^\circ)$ .

Ignoring the reduction of sensor sensitivity to oblique impacts by using Eqs. (8) and (9) will result in a hypothetical drop size distribution with too many small and not enough big drops. As a matter of fact signals generated by oblique hits correspond to those generated by smaller but normal impacting drops. Therefore, by taking such drop size distributions to calculate further rain parameters, for example, rain rates, results will be too small in comparison to real data. In case of heavy rain this deviation is about 34% (Förster 1998).

FIG. 8. Zone division considering signal reduction with decreasing impact angle. Zone 1: area of nearly normal impacts ( $90^\circ \geq \beta > 60^\circ$ ). Zone 2: area of oblique impacts ( $60^\circ \geq \beta > 30^\circ$ ). Zone 3: area of tangential impacts ( $30^\circ \geq \beta$ ).

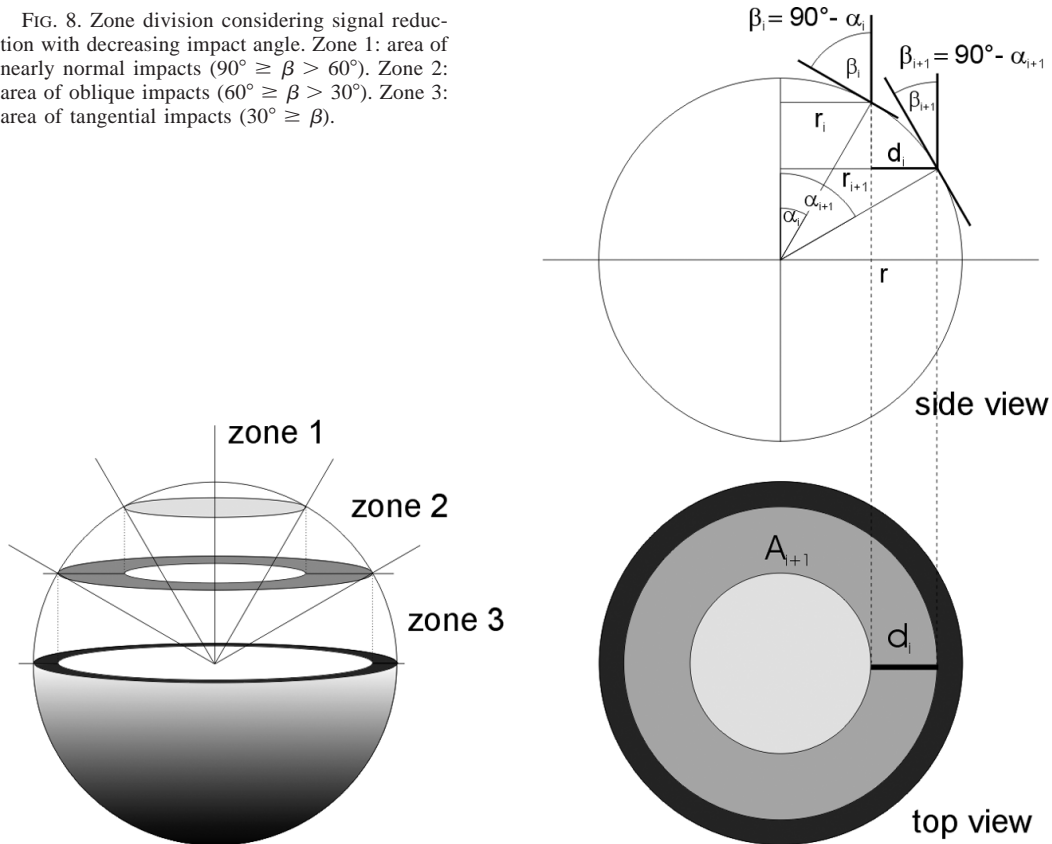




TABLE 4. Zones of 10° instance results with area ratios  $A_i/A$ .

$A_1/A$	$A_2/A$	$A_3/A$	$A_4/A$	$A_5/A$	$A_6/A$	$A_7/A$	$A_8/A$	$A_9/A$
0.03	0.09	0.13	0.16	0.18	0.16	0.13	0.09	0.03

This characteristic is analyzed more clearly. For simplification the following assumptions are made: first, a constant drop size of  $D = 3$  mm; second, terminal drop velocity, no wind; and third, a uniform distribution of drops in space. The rain rate  $R$  then is given by

$$R = \frac{NV_{\text{drop}}}{At_{\text{Int}}}, \quad (11)$$

with  $N$  the number of drop impacts per sensor cross section per observation time  $t_{\text{Int}}$ ,  $V_{\text{drop}}$  the drop volume, and  $A$  the sensor cross section.

Assuming a drop rate of 5 drops per second per sensor cross section and an observation time  $t_{\text{Int}} = 60$  s. Then about  $N = 300$  drops will impact equally distributed over the sensor cross section  $A = 15.9 \text{ cm}^2$ . With Eq. (11) the rain rate amounts to

$$R = \frac{NV_{\text{drop}}}{At_{\text{Int}}} = \frac{300 \left( \frac{\pi}{6} \right) D^3 (60)}{1.59(10^{-3})} [\text{mm h}^{-1}]$$

$$= 160 [\text{mm h}^{-1}]. \quad (12)$$

Uniform distribution of the drops across the sensor cross section results in a drop density of about 0.19 drops  $\text{mm}^{-2}$ , that is, one drop  $(5.3 \text{ mm}^2)^{-1}$ .

If the sphere is divided in sections of different drop impact angles, then for each of these sections drop rates and mean sensor signals can be determined. Figure 8, for example, shows such a zone division into three sections:

Zone 1, an area of nearly normal impacts	$90^\circ \geq \beta > 60^\circ$ ;
Zone 2, an area of oblique impacts	$60^\circ \geq \beta > 30^\circ$ ; and
Zone 3, an area of nearly tangential impacts	$30^\circ \geq \beta$ .

Projection of these zones into the horizontal plane provide their contributions  $A_i$  to the sensor cross section  $A$ . The projection areas  $A_i$ , that is, the circle and the circle ring areas are given by

$$\tilde{d}_i = \tilde{r}_{i+1} - \tilde{r}_i \quad (13)$$

TABLE 5. Cross section drop rates for the zones in Table 4.

Zone	1	2	3	4	5	6	7	8	9
Drop rates ( $\text{min}^{-1}$ )	9	27	39	48	51	48	39	27	9

$$\tilde{r}_i = \tilde{r} \sin(\alpha_i) \quad (14)$$

$$A_i = \pi \tilde{r}_{i+1}^2 - \pi \tilde{r}_i^2$$

$$= \pi \tilde{r}^2 [\sin^2(\alpha_{i+1}) - \sin^2(\alpha_i)] \quad (15)$$

$$A = \pi \tilde{r}^2 = \sum_i A_i, \quad (16)$$

with  $\tilde{d}_i$  the width of the circle rings,  $\tilde{r}_{i+1}$  the outer radius of a circle ring,  $\tilde{r}_i$  the inner radius of a circle ring, and  $\tilde{r}$  the radius of the sensor cross section.

Ratios of the projection areas  $A_i$  and the sensor cross section  $A$  amount to

$$\frac{A_i}{A} = \frac{\pi \tilde{r}_{i+1}^2 - \pi \tilde{r}_i^2}{\pi \tilde{r}^2} = \frac{\pi \tilde{r}^2 [\sin^2(\alpha_{i+1}) - \sin^2(\alpha_i)]}{\pi \tilde{r}^2}$$

$$= \sin^2(\alpha_{i+1}) - \sin^2(\alpha_i). \quad (17)$$

A division into zones of 10° for instance results in nine zones with the area ratios  $A_i/A$  shown in Table 4.

With these ratios and a mean drop density of about 5.3 drops  $\text{mm}^{-2}$  distributed uniformly over the sensor, cross section drop rates for each zone can be calculated, as shown in Table 5.

The sensitivity for normal or oblique drop impacts, hitting on the sensor surface (Fig. 3), is approximately given by the following equation:

$$U = U_0 [\cos(\alpha) + a\alpha^3 \sin(\alpha)], \quad (18)$$

with  $a = 0.0516$  and  $\alpha$  the angle of impact according to Fig. 8.

For the drop diameter  $D = 3$  mm and normal impact according to Eq. (8) the signal is  $U_{\text{max}}(D, 90^\circ) = 0.085 D^{2.5} = 1.325 \text{ V}$ . Corresponding output signals  $U_i$  for the other zones can be estimated using Eq. (18). Applying only the transfer function for normal impact condition corresponding drop sizes  $\tilde{D}_i$  can be attributed to these signals. Based on this hypothetical drop size distribution, an apparent rain rate  $\tilde{R}$  can be calculated by adding up the contributions  $\tilde{R}_i$  of all zones (Table 6).

The hypothetical rain rate  $\tilde{R}$  amounts to 104.5  $\text{mm h}^{-1}$ . In comparison with the correct value of rain rate of about 160.4  $\text{mm h}^{-1}$  this makes a deviation of 34%. Therefore, to minimize this deviation the impact angle dependency of the transfer function has to be considered

TABLE 6. Rain rate  $\tilde{R}_i$  from the contributions of all the zones.

Zone	1	2	3	4	5	6	7	8	9
$U_i/U_0$	0.996	0.966	0.908	0.826	0.725	0.611	0.491	0.371	0.255
$U_i$ (V)	1.320	1.280	1.203	1.094	0.961	0.810	0.651	0.492	0.338
$\tilde{D}_i$ (mm)	3.00	2.96	2.89	2.78	2.64	2.46	2.26	2.02	1.74
$\tilde{R}_i$ ( $\text{mm h}^{-1}$ )	4.80	13.84	18.60	20.38	18.54	14.12	8.89	4.40	0.94

in signal postprocessing. How this was done is described below.

Drop impacts generate output signal pulses  $U$  according to Eq. (18). In our case these pulses are recorded over time intervals of 1 min and are attributed to 20 signal classes in accordance with the classification performed for the Joss–Waldvogel disdrometer. Assuming a stationary uniform distribution of drops in the vicinity of the rain sensor for 1-min recording periods, the estimating method for a drop size classification was realized as follows.

In a first approximation each drop rate of the 20 signal classes  $K$  represents a combination of three drop groups  $i$ , with mean drop sizes  $D_{Ki}$ :

Group 1: normal, or nearly normal impacts

$$D_{K1} \quad (25\% \text{ of } A);$$

Group 2: oblique impacts

$$D_{K2}: D_{K2} > D_{K1} \quad (50\% \text{ of } A);$$

Group 3: tangential, or nearly tangential impacts

$$D_{K3}: D_{K3} > D_{K2} > D_{K1} \quad (25\% \text{ of } A).$$

Drop rates of each group are given by redistributing accumulated counts of the signal classes. These counts are divided in three parts defined by areas the zones have in relation to the whole cross section  $A$  (Fig. 8). About 25% of the counts in each signal class is the number of drops, which correspond to group 1, represented by normal, or nearly normal impacts. With Eq. (8) this number is attributed to a specific drop size class. The number of drops relating to group 2 (50% of the counts) and also group 3 (25% of the counts) are calculated in the same way: first, considering the sensor sensitivity for oblique, respectively, tangential impacts according to Eq. (18); and second, applying Eq. (8) to assign a specific drop size class. This evaluation is an approximation to the real drop size distribution taking into account the spherical shape of the piezoelectrical sensor.

The ability of this method to estimate drop size distribution is discussed for three different rain conditions:  $R_1 = 12 \text{ mm h}^{-1}$ , heavy rain;  $R_2 = 4.5 \text{ mm h}^{-1}$ , moderate rain; and  $R_3 = 0.75 \text{ mm h}^{-1}$ , light rain. Using the Marshall–Palmer drop size distribution, drop intensities can be calculated dependent on drop sizes. Based on this quantity drop rates referring to the sensor cross section are given and drop intensities can be determined with respect to drop size category.

As described for 3-mm drops above, similar calculations have to be performed for all drop size categories.

Drop intensity per drop class  $I_K$  and sensor cross section  $A$  is given by integrating the Marshall–Palmer drop size distribution and taking into account an observation period  $t_{\text{int}}$  of 1 min:

TABLE 7. Determination of rain rate based on Marshall–Palmer drop size distribution without and with consideration of the sensor sensitivity characteristic.

Rain rate (mm h <sup>-1</sup> )	Without		With	
	(mm h <sup>-1</sup> )	Deviation (%)	(mm h <sup>-1</sup> )	Deviation (%)
12	9.43	-21	12.35	+3
4.5	3.62	-19	4.74	+5
0.75	0.60	-20	0.78	+4

$$I_K(D_{Kl}, D_{Ku}) = v_{K\text{term}} A t_{\text{int}} \int_{D_{Kl}}^{D_{Ku}} N_0 e^{-\Lambda D} dD \quad (19)$$

$$I_K(D_{Kl}, D_{Ku}) = \frac{v_{K\text{term}} A t_{\text{int}} N_0}{\Lambda} (e^{-\Lambda D_{Kl}} - e^{-\Lambda D_{Ku}}), \quad (20)$$

with

$D_{K1}$ : lower limit of drop diameter for drop size class  $K$ ,

$D_{Ku}$ : upper limit of drop diameter for drop size class  $K$ ,

$\Lambda$ : exponent of the MP distribution,

$N_0 = 8000 \text{ mm}^{-1} \text{ m}^{-3}$ ,

$v_{K\text{term}}$ : terminal velocity for the mean drop diameter of each drop class  $(D_{K1} + D_{Ku})/2$ .

By ignoring the spherical sensor shape and its sensitivity characteristic drop rates of the lowest drop classes (representing small drops) will be too high in comparison to drop rates of the higher classes (big drops). Thus, rain rates will deviate up to 21% from actual rates if only the normal impact relation Eq. (8) is applied to the drop rates  $I_K$  to calculate rain rates (Table 7).

On the other hand, the deviation is reduced to 5% when taking into account the sensitivity characteristic of the sensor. Corresponding distributions are shown in Fig. 9. Beside the input datasets  $I_K$ , which were calculated using Eq. (20), results are presented that ignore respectively considering the sensitivity characteristic of the sensor with respect to Eq. (18).

Thus, taking into account the sensitivity characteristic of the spherical-formed sensor mean rain parameter can be estimated:

- drop intensity,
- drop size distribution,
- rain rate, and
- momentum flux.

In order to relate rain parameter to horizontal standard area, the wind influence on drop incidence angle has to be considered. For each drop size, or category, wind-dependent projections  $A_{KE}$  of the sensor cross section  $A$  exist in the horizontal plane. These projections are ellipses as presented in Fig. 10. Thus, an increase of terminal velocity  $v_{\text{term}}$  with drop size at constant wind will result in a decrease of the projected area. For a given



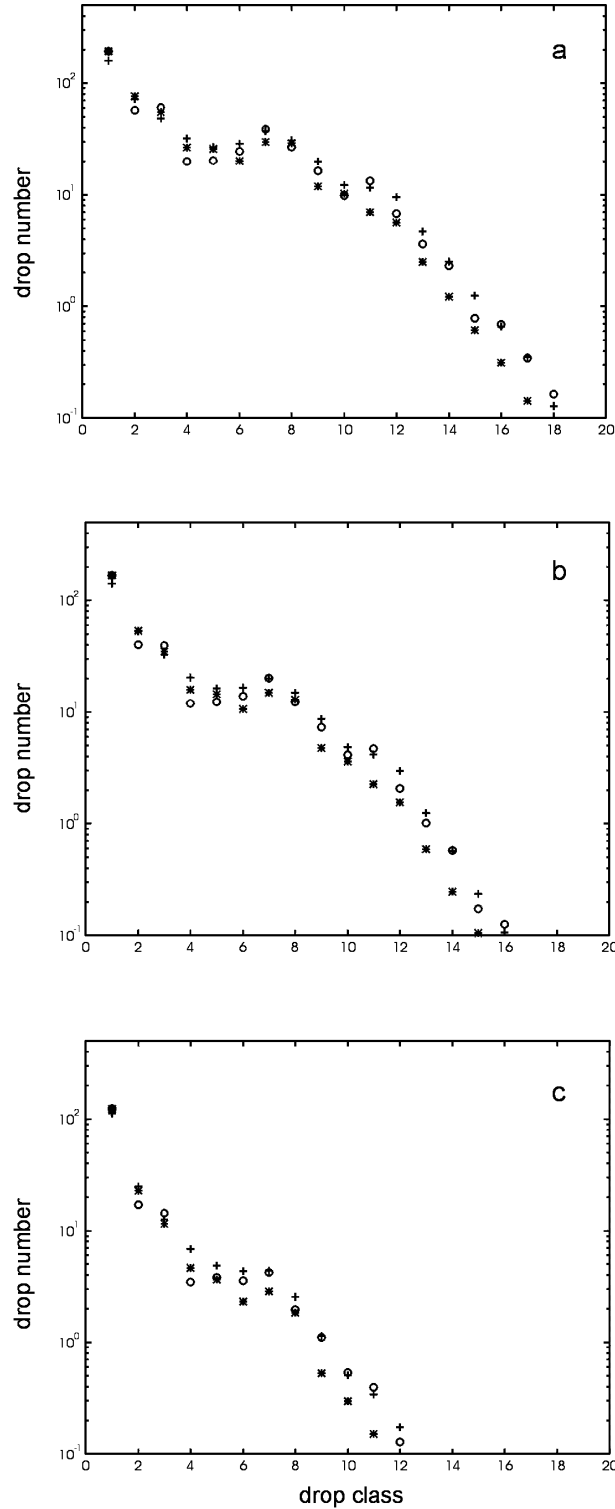


FIG. 9. Drop intensities based on Marshall–Palmer drop size distributions for three different intensities (a)  $R_1 = 12 \text{ mm h}^{-1}$ , heavy rain; (b)  $R_2 = 4.5 \text{ mm h}^{-1}$ , moderate rain; and (c)  $R_3 = 0.75 \text{ mm h}^{-1}$ , light rain. Symbols are as follows: +, distribution of input dataset according to Eq. (20); \*, analysis without consideration of the sensor's sensitivity characteristic; and  $\circ$ , analysis with consideration of the sensor's sensitivity characteristic.

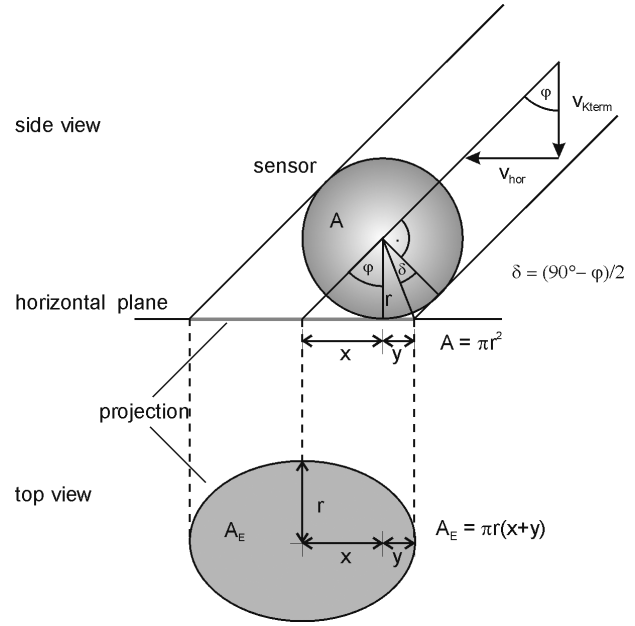


FIG. 10. Projection area  $A_E$  of the sensor cross section  $A$  in the horizontal plane for a wind speed  $v_{\text{hor}}$  and a given drop size category  $K$  characterized by a terminal velocity  $v_{K\text{term}}$ .

drop size category  $K$ , characterized by the terminal velocity  $v_{K\text{term}}$ , the ratio  $A_{KE}$  to  $A$  is

$$\frac{A_{KE}}{A} = \frac{1}{\cos(\phi)} = \sqrt{1 + \tan^2(\phi)} = \sqrt{1 + \frac{v_{\text{hor}}^2}{v_{K\text{term}}^2}}. \quad (21)$$

If  $N_K$  is the drop number corresponding to the drop size category  $K$ , which has been detected during the time period of analysis  $t_{\text{Int}}$ , then the drop intensity, the rain rate, and the momentum flux can be derived as follows.

The drop intensity  $T_R$  is the sum of drop intensities  $T_{KR}$  over all drop size categories  $K$ :

$$T_R = \sum_K T_{KR} = \sum_K \frac{N_K}{t_{\text{Int}} A_{KE}} \quad [\text{drops m}^{-2} \text{ s}]. \quad (22)$$

The rain rate  $R$  is given by

$$R = \sum_K R_K = \sum_K \frac{\pi D_K^3 N_K}{6 t_{\text{Int}} A_{KE}} \quad [\text{mm h}^{-1}]. \quad (23)$$

The horizontal momentum flux  $M_{\text{hor}}$  is

$$M_{\text{hor}} = \sum_K M_{K\text{hor}} = \sum_K \frac{\pi D_K^3 N_K v_w}{6 t_{\text{Int}} A_{KE}} \quad [\text{N m}^{-2}], \quad (24)$$

and the vertical momentum flux  $M_{\text{ver}}$  is

$$M_{\text{ver}} = \sum_K M_{K\text{ver}} = \sum_K \frac{\pi \rho D_K^3 N_K v_{K\text{term}}}{6 t_{\text{Int}} A_{KE}} \quad [\text{N m}^{-2}]. \quad (25)$$

In our application the parameter setting was  $t_{\text{Int}} = 1 \text{ min}$  and  $K = 1 \dots 20$ , according to settings that are used for impact-type rain sensors, like the Joss–Waldvogel disdrometer.

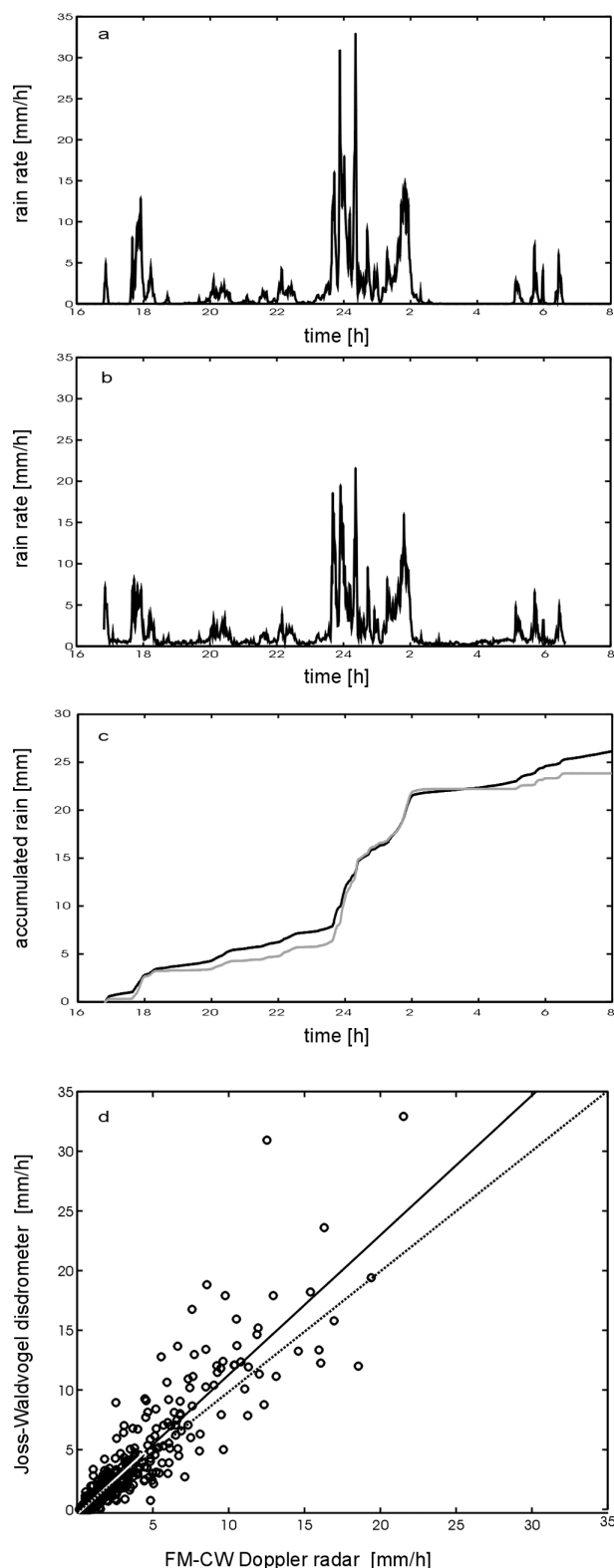


FIG. 11. Comparison of rain rates (analysis interval is 1 min): (a) rain rates, Joss–Waldvogel disdrometer; (b) rain rates, FM–CW Doppler radar; and (c) accumulated rain, sum curves of (a) and (b), where the gray line is the Joss–Waldvogel disdrometer, and the black line is the FM–CW Doppler radar. (d) Scatterplot

## 5. Piezoelectrical rain gauge: Validation

The applicability of the piezoelectrical rain sensor was verified during a campaign by comparing the results with those provided from different conventionally used rain sensors. Furthermore, the objective was to test extended characteristics, such as the influence of ambient noise and wind fluctuations. The types of rain gauges that have been compared in this experiment are a Joss–Waldvogel disdrometer RD 69 (Joss and Waldvogel 1967, 1969), a FM–CW Doppler radar (Richter 1994a,b), a ship rain gauge SRM 450 (Hasse and Großklaus 1993; Hasse et al. 1994; Großklaus 1995), and a piezoelectrical rain gauge S-1012-1.5" (Förster 1998, 1999). While the piezoelectrical rain gauge has been developed primarily for rain measurements on buoys, the ship rain gauge (Hasse et al. 1998) enables rain-rate measurements from a moving ship. As with conventional rain gauges it has a horizontal orifice. Additionally it is equipped with a lateral drop collector that measures the wind-dependent water amount driven against the side of the gauge. The water amounts intercepted at the top and the side are collected separately, and each is measured by forming calibrated drops in a dispense unit. These drops are counted when they pass through a light barrier. The water amounts are thus converted to electronic counts for recording. Together with data gathered from a cup anemometer, corrected rainfall rates are obtained as a wind speed-dependent weighted average.

The experiment had been conducted at a land-based test site on the airfield of Hohenweststedt in the northern part of Germany during the period May–August 1994. To minimize spatial and temporal deviation of rain rate and drop size distribution, the instruments were installed close to each other within an area of  $15 \text{ m} \times 15 \text{ m}$ , without causing any instrument interference. During the experiment period, the most spectacular rain event was a thunder shower lasting 10.5 h with a strong variation of rain intensity. Rain rates measured by the Joss–Waldvogel disdrometer were taken as the reference for rain gauge comparison (Fig. 11). Rain started at 1648 UTC on 4 July 1994. The maximum intensity with rain rates above  $30 \text{ mm h}^{-1}$  occurred at 2353 UTC and 0021 UTC on 5 July. The mean wind velocity was  $1.76 \text{ m s}^{-1}$  with a maximum of about  $3.0 \text{ m s}^{-1}$  and a standard deviation of  $0.81 \text{ m s}^{-1}$ .

In Figs. 11–13 rain rates of the piezoelectrical and the other rain gauges are compared with the results of the Joss–Waldvogel disdrometer. The interval for calculating rain parameters was 1 min for the Joss–Waldvogel disdrometer, the FM–CW Doppler radar, and the piezoelectrical rain gauge, whereas 2-min intervals had been chosen for the ship rain gauge data analysis.

←

of curves (a) and (b), where the dotted line is the 1:1 line, the black line is the linear regression, and the correlation coefficient amounts to  $r = 0.92$ .

In addition to the time series of rain rates, corresponding scatterplots of the FM–CW Doppler radar, the ship rain gauge, and the piezoelectrical rain gauge with reference to the Joss–Waldvogel disdrometer are presented in Figs. 11–13.

Deviations in rain rate have different reasons, mainly the temporal and local variability of rain and wind speed in addition to sensor characteristics. On the average the sensor systems provide similar results. Deviations in rain rates between the FM–CW Doppler radar and those of the other rain gauges might be due to the different locations of observations, which in case of the radar was in about 250-m height above the ground. In comparison, rain rates deduced from radar recordings were up to  $10 \text{ mm h}^{-1}$  less than that of the Joss–Waldvogel disdrometer (Fig. 11). The higher sensitivity of the disdrometer, especially in heavy rain periods, is given by the scatterplot in Fig. 11d. The regression line was computed using the method of least squares and has a correlation coefficient of 0.92.

Results of the Joss–Waldvogel disdrometer and the ship rain gauge are in close agreement, yielding a correlation coefficient of 0.96 (Fig. 12).

Comparison of the Joss–Waldvogel disdrometer and the piezoelectrical rain gauge in Fig. 13 provides good results, too. During light rain rates the Joss–Waldvogel disdrometer seems to be a bit more sensitive. In moderate and heavy rain activity both devices give comparable results (Figs. 13a–c). This agreement is reflected in the scatterplot shown in Fig. 13d. The fitted curve has a slope of nearly unity, with a correlation coefficient of 0.94.

Thus, the new rain sensor permits us to obtain and analyze in situ measurements of rain at sufficient resolution, which are otherwise very difficult to perform on buoys at sea.

A restriction of the piezoelectrical rain gauge is its small drop detection limitation. The threshold was determined by recordings that were performed under different wind conditions. Only drop sizes with diameters  $D > 0.5 \text{ mm}$  can be separated from ambient noise and are detectable using the rain gauge type S-1012-1.5" (Förster 1998). In comparison, the Joss–Waldvogel disdrometer permits measurements of drops down to  $D = 0.3 \text{ mm}$  (Joss and Waldvogel 1967, 1969).

## 6. Taking the piezoelectrical rain gauge to sea

The objectives we hoped to achieve with the first rain measurements on a buoy system were the classification of rain and the identification of rainfall-dependent parameters very close to the sea surface, and the ensuing effects on the air–sea interface and consequently on remote sensing.

### a. Implementation of the piezoelectrical rain gauge on a drift buoy system—In situ measurements

In order to execute measurements of surface roughness variations by rain, a free drifting buoy system is

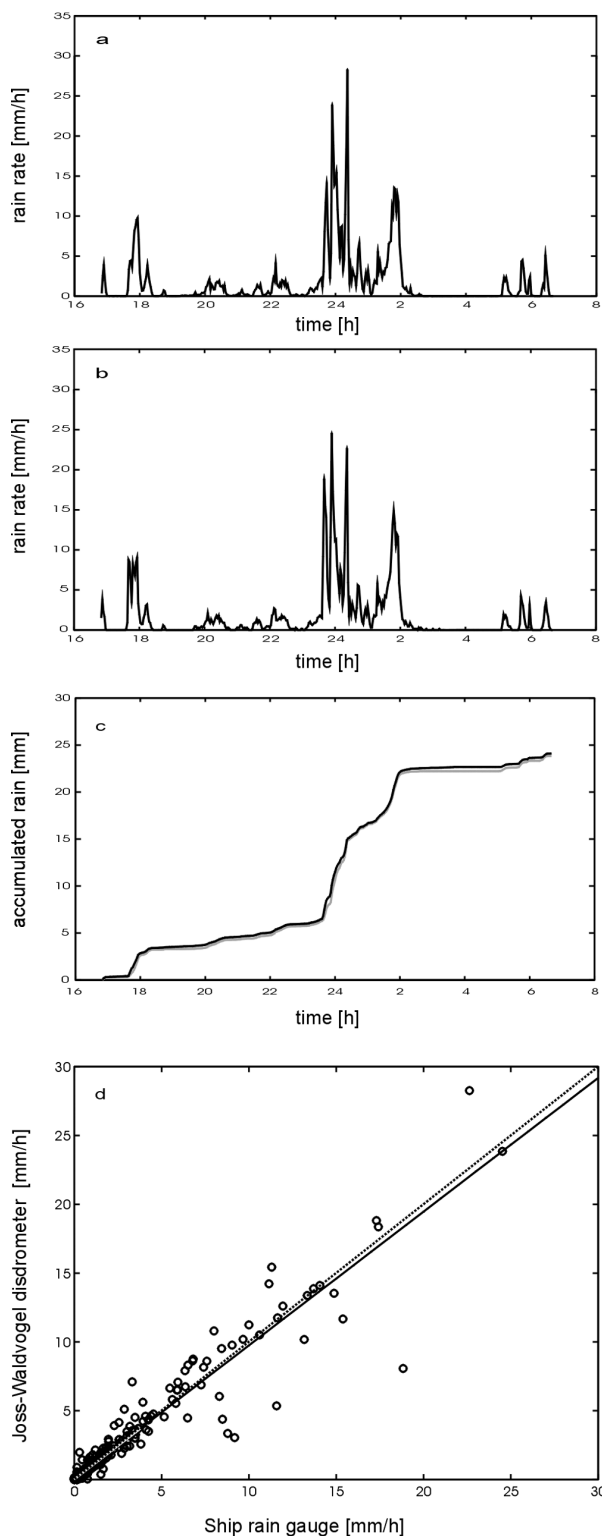


FIG. 12. Comparison of rain rates (analysis interval is 2 min): (a) rain rates, Joss–Waldvogel disdrometer; (b) rain rates, ship rain gauge SRM 450; and (c) accumulated rain, sum curves of (a) and (b), where the gray line is the Joss–Waldvogel disdrometer, and the black line is the ship rain gauge SRM 450. (d) Scatterplot of curves (a) and (b), where the dotted line is the 1:1 line, the black line is the linear regression, and the correlation coefficient amounts to  $r = 0.96$ .

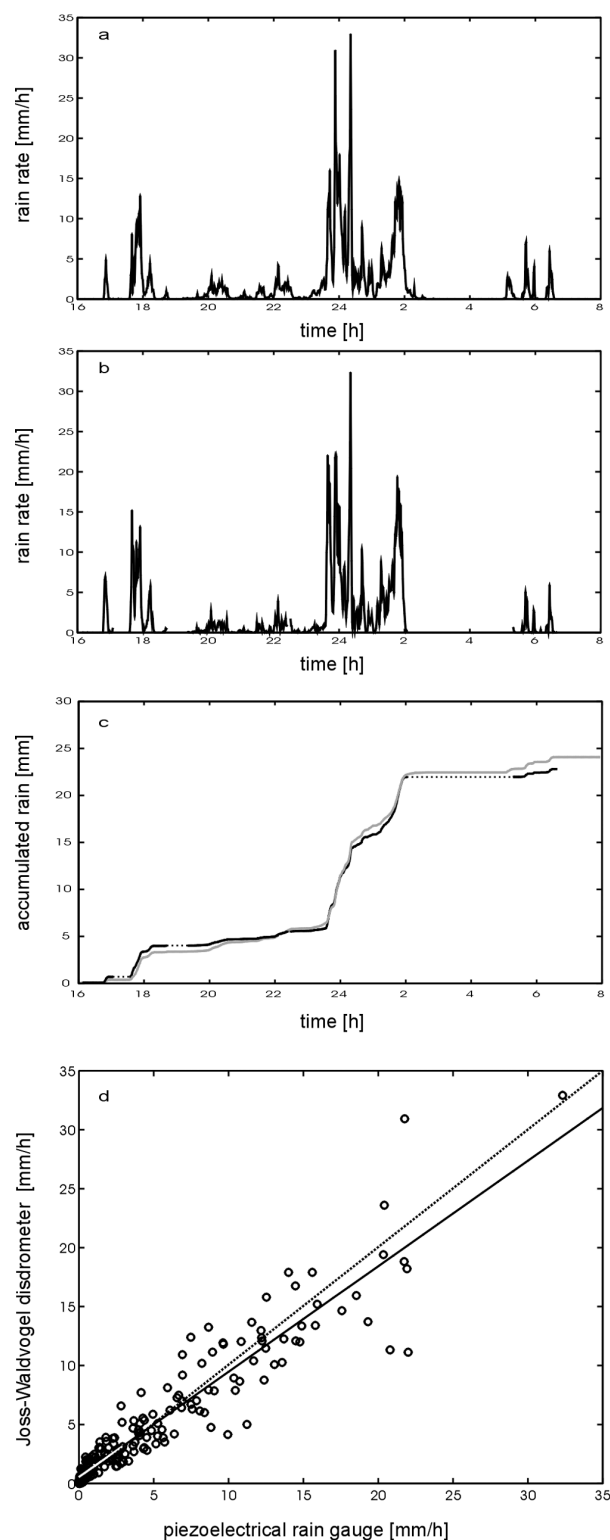


FIG. 13. Comparison of rain rates (analysis interval is 1 min): (a) rain rates, Joss-Waldvogel disdrometer; (b) rain rates, piezoelectrical rain gauge (broken line = interrupted recording); (c) accumulated rain, sum curves of (a) and (b); where the gray line is the Joss-Waldvogel disdrometer, and the black line is the piezoelectrical rain gauge (broken line = interrupted recording). (d) Scatterplot of curves

used (Stolte 1994). Figure 14a shows a sketch of the buoy and its instrumentation. Based on the hydrodynamic characteristics of the buoy, which follows the local currents, precise measurements of short-scale waves along long-wave profiles are feasible.

The FWG Air-Sea Interaction drift buoy is equipped with a resistance wire gauge for short-wave measurements in addition to the newly developed rain sensor and other sensors as identified on a photo (Fig. 14b). All sensor elements mounted above the water line are visible. On top of the buoy a cup and a sonic anemometer (A) are placed for wind and turbulence measurements. In front, a resistance wire gauge (B) is installed for short-scale roughness measurements. Close to this location, the piezoelectrical rain sensor (C) is mounted.

#### b. *In situ investigations of rain-related sea surface effects*

In addition to the rain-induced wave damping process drop impacts increase the short-scale roughness at the sea surface particularly in low-wind situations (Yakimov 1959; Houk and Green 1976; Le Méhauté 1988, 1990; Tsimplis 1990, 1992; Bliven et al. 1997; Förster 1998, 1999; Braun et al. 1999; Craeye et al. 1999).

During a thunder shower with maximum rain rate of  $27 \text{ mm h}^{-1}$ , simultaneous measurements of rain rate, drop intensity, and rain-generated surface roughness were obtained by the buoy (Förster 1998). Throughout the period of observation, the wind speed was less than  $1.7 \text{ m s}^{-1}$  and below the initial condition for generation of wind waves (Stolte 1988, 1996). Thus, the measured sea surface roughness was the result of rain only. Wave energy density spectra are shown in Fig. 15 for different rain rates.

The energy densities of sea surface waves reveal that they are very sensitive to rain impact variations. While an increase of rain rate from  $1$  to  $16.7 \text{ mm h}^{-1}$  causes significant roughness enhancement (curves A–C), a balance between wave damping and roughness generation results in a constant energy density when the rain intensity further rises from  $16.7$  to  $22.6 \text{ mm h}^{-1}$  (curves C–E).

As illustrated in Fig. 15, the rain-induced roughness effects a broad frequency band from  $3$  to  $30 \text{ Hz}$  and wavelengths between  $17$  and  $0.7 \text{ cm}$ , respectively. It covers the X-, C-, and L-band radar scatterers, the base for ocean radar remote sensing (e.g., C-band of the European Remote-Sensing satellites *ERS-1*, *ERS-2*, and *ENVISAT*). The backscatter of these radar wavelengths is consequently strongly affected by rain-induced sea

(a) and (b) (time interval 22:31 – 02:05), where the dotted line is the 1:1 line, the black line is the linear regression, and the correlation coefficient amounts to  $r = 0.94$ .

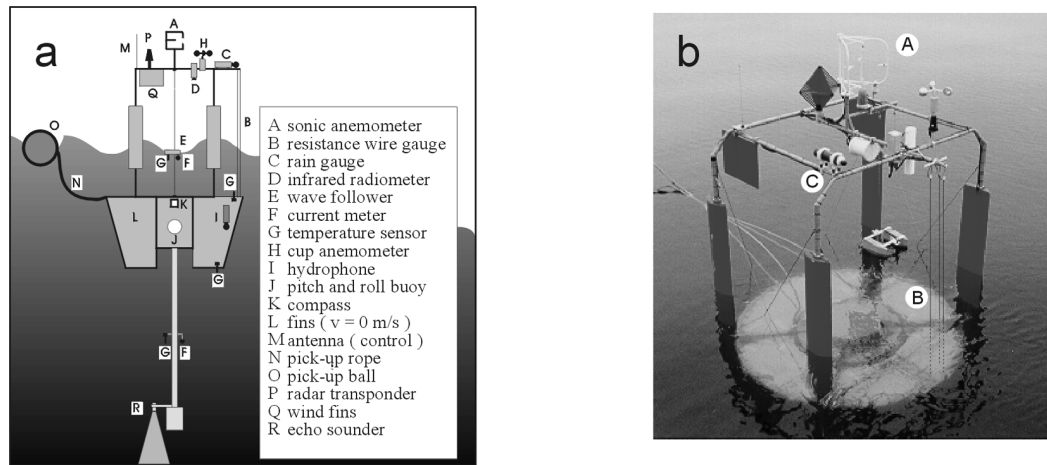


FIG. 14. FWG Air-Sea Interaction Drift Buoy System: (a) instrumentation and (b) system during deployment operation procedure.

surface roughness variations (Melsheimer 1998; Melsheimer et al. 1999).

## 7. Conclusions

A piezoelectrical rain gauge has been developed that is suitable for use on buoys under calm and rough environmental conditions. It is based on a principle re-

quiring no moving components. This is ideal for long time exposure without maintenance. Rubber coating of the sensor provides seawater resistance and negligible fouling. This is a basic requirement for long time reliable operation, even after contact with seawater by submergence and spray. Especially when used at oceanic sites, it permits rain measurements just above the sea surface. In order to estimate rain-related parameters from drop-induced sensor signals, it was shown that wind, vertical up- and downdrafts, and the sensitivity characteristic of the piezoelectric rain sensor have to be taken into account. Based on this information results of drop intensity, drop size distribution, rain rate, and rain momentum flux can be estimated.

This information is needed to better understand rain-induced sea surface processes like damping of sea waves, short-scale roughness enhancement, and generation of underwater ambient noise, processes that affect the quality of radar and sonar remote sensing methods.

**Acknowledgments.** The piezoelectrical rain gauge was developed through the efforts of Prof. Dr. Peter Wille. Engineering and technical support was provided by Dr. Broder Fedders, Wolfgang Waeber, and Hans-Peter Westphal, FWG, Kiel, Germany. The Joss-Waldvogel Disdrometer and the FM-CW Doppler Radar were operated by Dr. Carolin Richter, Max-Planck Institute für Meteorologie, Hamburg, Germany. The ship rain gauge support was provided by Dr. Martin Großklaus, Institut für Meereskunde, Kiel, Germany. This work was part of the Ph.D. thesis research at TUHH.

## APPENDIX

### Notation

$a$	calibration coefficient
$A A_{KE}$	sensor cross section, projection of the sensor cross section into the horizontal plane for drop size category $K$

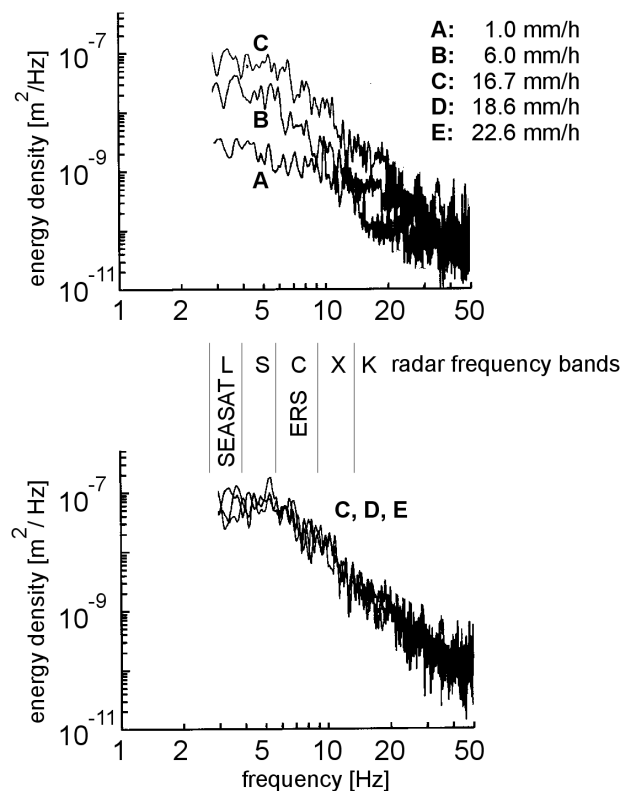


FIG. 15. Energy density spectra of sea surface waves (height) depending on rain intensity for 1.0, 6.0, 16.7, 18.6, and 22.6  $mm h^{-1}$ .



$C_s$	sensor capacity
$d$	dielectric constant
$\tilde{d}_i$	width of cicle ring
$D \tilde{D}_i$	drop diameter, apparently drop diameter in relation of zone $i$
$D_K D_{Kl} D_{Ku}$	mean, lower, upper drop diameter of drop size category $K$
$E_{ac} E_{kin}$	acoustical, kinetic energy
$F F_d$	force, drag force
$f$	momentum transfer function
$g$	gravity acceleration
$h$	fall height
$I_K$	drop intensity per drop class $K$
$K$	drop size category
$m$	mass
$M_{hor} M_{ver}$	horizontal, vertical momentum flux due to rain impact
$M_{Khor} M_{Kver}$	contribution of drop size category $K$ to the horizontal, vertical momentum flux
$N N_K$	drop number, drop number of drop size category $K$ measured by the rain sensor during basic recording time unit $t_{int}$
$N_0$	coefficient of Marshall–Palmer drop size distribution ( $N_0 = 8000 \text{ mm}^{-1} \text{ m}^{-3}$ )
$p$	momentum
$R R_K \tilde{R}$	rain rate, rain rate contribution of drop size category $K$ , apperently rain rate
$r$	correlation coefficient
$\tilde{r}$	radius
$t t_{int}$	time, time period of analysis
$T_{KR}$	drop intensity contribution of drop size category $K$
$T_R$	drop intensity, sum of $T_{KR}$ over all drop size categories $K$
$U U_{max}$	sensor voltage output, maximum voltage output in case of normal drop impact
$V$	voltage
$V_{drop}$	drop volume
$v v_{hor} v_{ver} v_{imp}$	velocity, horizontal drop velocity, vertical drop velocity, drop impact velocity
$v_{term} v_{Kterm}$	terminal velocity, mean terminal velocity of drops in size category $K$
$v_w v_z$	wind speed, up- and downdraft
$\alpha \beta \delta \varphi$	angles
$\gamma$	drag coefficient
$\Lambda$	exponent of Marshall–Palmer drop size distribution
$\Delta p$	momentum transferred due to drop impact
$\Delta U_{int}$	change of integrated sensor signal
$\rho$	density of drop fluid

## REFERENCES

- Atlas, D., R. C. Srivastava, and R. S. Sekhon, 1973: Doppler radar characteristics of precipitation at vertical incidence. *Rev. Geophys. Space Phys.*, **11**, 1–35.

- Bliven, L. F., P. W. Sobieski, and C. Craeye, 1997: Rain generated ring-waves: Measurements and modeling for remote sensing. *Int. J. Remote Sens.*, **18**, 221–228.
- Braun, N., M. Gade, and P. A. Lange, 1999: Radar backscattering measurements of artificial rain impinging on a water surface at different wind speeds. *Proceedings of IGARSS'99 Hamburg Germany: IEEE 1999 International Geoscience and Remote Sensing Symposium*, IEEE, CD-ROM.
- Caldwell, R. C., and W. P. Elliott, 1971: Surface stresses produced by rainfall. *J. Phys. Oceanogr.*, **1**, 145–148.
- Channel Industries, Inc., 1995: *Piezoelectric Ceramics*. Channel Industries, Inc., 15 pp. [Available from Channel Industries, Inc., 839 Ward Drive, Santa Barbara, CA 93111.]
- Craeye, C., 1998: Radar signature of the sea surface perturbed by rain. Ph.D. thesis, Université Catholique de Louvain 313 pp.
- , P. W. Sobieski, and L. F. Bliven, 1999: Radar signature of the sea surface perturbed by rain. *Proceedings of IGARSS '99 Hamburg Germany: IEEE 1999 International Geoscience and Remote Sensing Symposium*, IEEE, CD-ROM.
- Förster, J., 1998: Erfassung des regeneinschlags auf see mit piezokeramischen sensoren. Ph.D. thesis, Technische Universität Hamburg-Harburg, Germany, 207 pp.
- , 1999: On the action of rain in calming the sea and generating sea surface roughness. *Proceedings of IGARSS '99 Hamburg Germany: IEEE 1999 International Geoscience and Remote Sensing Symposium*, IEEE, CD-ROM.
- Großklaus, M., 1995: Niederschlagsmessung auf dem Ozean von fahrenden Schiffen. Ph.D. thesis, Christian-Albrechts-Universität zu Kiel, 115 pp.
- Gunn, R., and G. D. Kinzer, 1949: The terminal velocity of fall for water droplets in stagnant air. *J. Meteor.*, **6**, 243–249.
- Hasse, L., and M. Großklaus, 1993: Measurement of precipitation at sea. *Precipitation Measurement and Quality Control*, B. Sevrulic and M. Lapin, Eds., Slovak Hydrometeorological Institute and ETH Zürich, 36–41.
- , —, H. J. Isemer, and K. Uhlig, 1994: New ship rain gauge. WMO Instruments and Observing Methods Rep. 57, WMO/TD-No. 588, 97–101.
- , —, and —, 1998: A ship rain gauge for use in high wind speeds. *J. Atmos. Oceanic Technol.*, **15**, 380–386.
- Houk, D., and T. Green, 1976: A note on surface waves due to rain. *J. Geophys. Res.*, **81**, 4482–4484.
- Hsiao, M., S. Lichter, and L. G. Quintero, 1988: The critical Weber number for vortex and jet formation for drops impinging on a liquid pool. *Phys. Fluids*, **31**, 3560–3562.
- Joss, J., and A. Waldvogel, 1967: Ein spektrograph für Niederschlagstropfen mit automatischer Auswertung. *Pure Appl. Geophys.*, **68**, 240–246.
- , and —, 1969: Raindrop size distribution and sampling size errors. *J. Atmos. Sci.*, **26**, 566–569.
- Le Méhauté, B., 1988: Gravity—Capillary rings generated by water drops. *J. Fluid Mech.*, **197**, 415–427.
- , 1990: Dynamic interaction of intense rain with water waves. *J. Phys. Oceanogr.*, **20**, 1805–1812.
- , S. Wang, and C. Lu, 1987: Cavities, domes and spikes. *J. Hydraul. Res.*, **25**, 583–602.
- Marshall, J. S., and W. M. Palmer, 1948: The distribution of raindrops with size. *J. Meteor.*, **5**, 165–166.
- Melsheimer, C., 1998: Signaturen von regen in radaraufnahmen des meeres. Ph.D. thesis, Universität Hamburg, Germany, 125 pp.
- , W. Alpers, and M. Gade, 1999: Simultaneous observations of rain cells over the ocean by the synthetic aperture radar aboard the ERS-1/2 satellites and by weather radars. *Proceedings of IGARSS'99, Hamburg Germany: IEEE 1999 International Geoscience and Remote Sensing Symposium*, IEEE, CD-ROM.
- Nystuen, J. A., J. R. Proni, P. G. Black, and J. C. Wilkerson, 1996: A comparison of automatic rain gauges. *J. Atmos. Oceanic Technol.*, **13**, 62–73.
- Ocean Research Technology, 1990: Simrad product information—

- ORT-Model S-1012-1½" Spherical hydrophone. SIMRAD Sub-sea A/S, 2 pp.
- PMS, 1989: Ground based precipitation probe PMS model GBPP-100 operating and servicing manual. Particle Measuring Systems Inc., 36 pp. [Available from Particle Measuring Systems Inc., 1855 South 57th Court, Boulder, CO 80301.]
- Pumphrey, H. C., and L. A. Crum, 1990: Free oscillations of near-surface bubbles as a source of the underwater noise of rain. *J. Acoust. Soc. Amer.*, **87**, 142–148.
- Richter, C., 1994a: Niederschlagsmessung mit dem vertikal ausgerichteten FM-CW-Dopplerradar-RASS-System-Validierung und Anwendung. Berichte aus dem Zentrum für Meeres- und Klimaforschung der Universität Hamburg, Reihe A: Meteorologie Nr. 12, 143 pp.
- , 1994b: Deriving rainfall parameters by using a Doppler RADAR-RASS system at vertical incidence. *Third Int. Symp. on Tropospheric Profiling: Needs and Technologies*, Hamburg, Germany, Max-Planck-Gesellschaft zur Förderung der Wissenschaften, 453–455.
- Skaar, J., 1955: On the measurement of precipitation at sea. *Geofys. Publ.*, **19**, 1–32.
- Spilhaus, A. F., 1948: Raindrop size, shape and falling speed. *J. Meteor.*, **5**, 108–110.
- Stolte, S., 1988: Short wave modulation and breaking, experimental results. *Proc. Workshop on Modulation of Short Wind Waves in the Gravity-Capillary Range by Non-Uniform Currents*. DeBilt, Netherlands, Royal Netherlands Meteorological Institute (KNMI), 201–210.
- , 1994: Short-wave measurements by a fixed tower-based and a drifting buoy system. *IEEE J. Oceanic Eng.*, **19**, 10–22.
- , 1996: Short waves and wave breaking, radar and sonar scatter. *Proc. Symp. on THE AIR-SEA INTERFACE Radio and Acoustic Sensing, Turbulence and Wave Dynamics*, Marseilles, France, The Rosenstiel School of Marine and Atmospheric Science, University of Miami, 651–658.
- Tsimplis, M., 1990: The attenuation of waves under the action of rain. Ph.D. thesis, University of Southampton, 236 pp.
- , 1992: The effect of rain in calming the sea. *J. Phys. Oceanogr.*, **22**, 404–412.
- Wang, T., and J. D. Crosby, 1993: Taking rain gauges to sea. *Sea Technol.*, **61**, 61–65.
- Winkler, P., 1993: Response of precipitation sensors to rain. *Meteor. Z.*, **2**, 35–44.
- Yakimov, J. L., 1959: Ursache der Wellenauslöschung durch Regen. *Izv. Sib. Otd. Akad. Nauk. USSR*, **5**, 125–126.

Copyright of Journal of Atmospheric & Oceanic Technology is the property of American Meteorological Society and its content may not be copied or emailed to multiple sites or posted to a listserv without the copyright holder's express written permission. However, users may print, download, or email articles for individual use.